Photoacoustics 23 (2021) 100278

Contents lists available at ScienceDirect

Photoacoustics

journal homepage: www.elsevier.com/locate/pacs

Research article

Classification and discrimination of real and fake blood based on photoacoustic spectroscopy combined with particle swarm optimized wavelet neural networks

Zhong Ren [a,b,*], Tao Liu [a], Guodong Liu [a,b]

[a] Key Laboratory of Optic-Electronic and Communication, Jiangxi Science and Technology Normal University, Nanchang, Jiangxi, 330038, China
[b] Key Laboratory of Optic-Electronic Detection and Information Processing of Nanchang City, Jiangxi Science and Technology Normal University, Nanchang, Jiangxi, 330038, China

ARTICLE INFO

Keywords:
Photoacoustic spectroscopy
Wavelet neural network
Particle swarm optimization
Correct rate
Blood

ABSTRACT

In this work, photoacoustic spectroscopy was employed to distinguish real blood from fake blood rapidly, accurately, and recoverably. To achieve this goal, a photoacoustic detection system for blood was established in the forward mode. In the experiments, four kinds of animal blood and two kinds of fake blood in a total of 150 groups were used. The time-resolved photoacoustic signal and peak-to-peak values (PPVs) of all blood were captured in 700−1064 nm with intervals of 5 nm. Experimental results show that the amplitudes, profiles, peak-point time, and PPVs are different between real and fake blood. Although the PPVs of real blood are larger than those of the fake ones at 700−850 nm, the differences in PPVs are not obvious at 850−1064 nm, especially when there are spectral overlaps of PPVs. To accurately classify and discriminate real and fake blood, a wavelet neural network (WNN) was used to train 120 groups of blood and test 30 groups of blood. Moreover, the particle swarm optimization (PSO) algorithm was used to optimize the weights and thresholds, as well as the translation and scale factors of the Morlet-liked wavelet basis function of the WNN. Under optimal parameters, the correct rate of the WNN-PSO algorithm was improved from 63.3% to 96.7%. Next, principal component analysis (PCA) was combined into the WNN-PSO algorithm to further improve the correct rate. The results indicate that the correct rate of the PCA-WNN-PSO algorithm with 10 principal components reaches 100 %. Therefore, photoacoustic spectroscopy combined with the PCA-WNN-PSO algorithm exhibits excellent performance in the classification and discrimination of real and fake blood.

1. Introduction

Blood is not only one of most important tissues in the biological body but it also plays a significant role in some fields, such as biomedical therapy, criminal investigation, and edible animal blood food. Due to the high economic added value, some events with abuse of blood have recently occurred. For example, it was reported that fake blood was used to forge and disturb the criminal scenes [1,2]. In animal inspection and quarantine, there have also been some cases of fake blood being used under the false pretence of being real blood. In addition, fake blood was used to produce counterfeit blood products. These events seriously threaten society stability and food safety. Therefore, the accurate detection and discrimination of real and fake blood is very urgent need in daily life.

Since fake blood looks like real blood from colour and morphology viewpoints, it is not easy to distinguish it by only visual inspection. For gas or liquid chromatography [3,4] and biochemical analysis [5], professional staff are needed to operate the instrument and analyse the detection results via professional knowledge, and the cost of these instruments is very expensive. In addition, pure spectral methods, such as near infrared spectroscopy, Raman spectroscopy, and fluorescence spectroscopy, were used to identify real and fake blood. Wan et al. [6] used infrared spectroscopy and the correlation coefficient method to recognize blood. The correlation coefficient between the same species of animals reached 0.99, but the correlation coefficient between different species of animals ranged from 0.50948 to 0.91613. Bai et al. [7]

* Corresponding author at: Key Laboratory of Optic-Electronic and Communication, Jiangxi Science and Technology Normal University, Nanchang, Jiangxi, 330038, China.
E-mail address: renzhong0921@163.com (Z. Ren).

https://doi.org/10.1016/j.pacs.2021.100278
Received 20 January 2021; Received in revised form 9 May 2021; Accepted 24 May 2021
Available online 1 June 2021

combined Raman spectroscopy with principal component analysis (PCA) to distinguish the blood attributions of animals and humans. The recognition rate between human and animal blood reached 95 %, and the recognition rate between animals reached 90 %. Mclaughlin et al. [8] employed Raman spectroscopy and a chemometric model to identify the origin of human and animal blood. Wang [9] combined Raman spectroscopy with a chemometric method to distinguish human blood from animal blood, and the recognition rate of human and animal blood was improved by extracting phase information from Raman spectra based on the Hilbert transform. Gao et al. [10] used fluorescence spectroscopy and a back propagation neural network (BPNN) to study the recognition and classification of animal blood. Lu [11] processed the fluorescence spectra of four kinds of animal blood (pigeon, chicken, mouse, sheep) by using wavelet denoising and feature extraction of discriminant statistics and used a support vector machine (SVM) algorithm to classify and discriminate the blood. Although the distinction of blood has already been studied by using pure spectral methods, the captured spectra of samples were easily interrupted by other components and scattering light. At the same time, spectral overlap is easily generated, which limits the accuracy of spectral detection. To overcome these drawbacks, the discrimination of real and fake blood was studied via a novel alternative method, i.e., photoacoustic spectroscopy, in this work. It is a promising, hybrid and non-invasive detection method that combines the advantages of pure optics and pure ultrasonics. More importantly, the problems of scattering light and spectral overlap can be overcome because the method captures ultrasonic signals rather than photons, which can improve the detection accuracy. To date, photoacoustic spectroscopy has already been used in biomedical diagnosis, e.g., blood glucose [12–14], blood oxygen [15–17], and tumor detection [18,19]. However, research on the classification and discrimination of real or fake blood by using photoacoustic spectroscopy has not been reported before.

In this work, to classify and discriminate real and fake blood via photoacoustic spectroscopy, a set of photoacoustic detection systems was established to obtain the photoacoustic signals of real and fake blood. In the system, a 532 nm pumped optical parameter oscillator (OPO) tunable pulsed laser was used as the excitation source, and a focused ultrasonic transducer was used to capture the photoacoustic signal of blood. In the experiments, six different kinds of blood, i.e., four kinds of animal blood (horse, cow, rabbit, and sheep) and two kinds of fake blood (props blood and red ink), were used as the experimental samples. The time-resolved photoacoustic signal and PPVs of all blood samples were obtained in the wavelength range 700−1064 nm with an intervals of 5 nm. To achieve highly accurate classification and discrimination of real and fake blood, a wavelet neural network (WNN) algorithm was employed. Meanwhile, a Morlet-liked wavelet basis function was used. Moreover, to improve the correct rate, the weights, thresholds, translation and scaling factors of the wavelet basis function of the WNN were optimized by the particle swarm optimization (PSO) algorithm. To obtain the optimal parameters of the WNN and WNN-PSO algorithms, the effects of neuron number in the hidden layer, two learning rate factors (η, λ), inertia weight, two acceleration factors (c_1, c_2), iteration times, and training times on the correct rates and mean square errors of classification and discrimination of the real and fake blood were all studied. The performances of the WNN and WNN-PSO algorithms were compared. To further improve the correct rate, the PCA algorithm was used to extract the characteristic information from the photoacoustic peak-to-peak spectra at full wavelengths, then, it was also coupled into the WNN-PSO algorithm, that is, the PCA-WNN-PSO algorithm was used. To obtain the optimal principal components, the effect of different principal components on the correct rate and mean square error was investigated. Under the optimal parameters, the correct rate of classification and discrimination of real and fake blood based on the PCA-WNN-PSO algorithm reaches 100 %.

There are three aims in this work. The first is to supply a novel alternative method of identifying real and fake blood. To achieve this purpose, a set of photoacoustic detection systems of blood was established to capture the time-resolved photoacoustic signal and peak-to-peak spectra of blood samples from visible light to near-infrared wavebands. The second is to compare and analyze the different properties of blood samples from the viewpoints of photoacoustic signals, as well as state the necessity of using the WNN algorithm to classify and distinguish real and fake blood. The third is to accurately classify and distinguish real blood and fake blood by using the WNN algorithm. More importantly, to further improve the correct rate, the WNN was optimized by PSO and combined with PCA, i.e., the PCA-WNN-PSO algorithm was used.

2. Theories

2.1. Photoacoustic spectroscopy

The basic mechanism of photoacoustic spectroscopy is the photoacoustic effect. When a beam of modulated laser with a short pulse (~ns) irradiates a sample, the temperature will be raised within a certain period time due to the absorbed energy in the irradiated region, which results in rapid volume expansion and then generates ultrasonic waves, i.e., the photoacoustic signal. In general, the photoacoustic effect can be described by a semi-quantitative formula [20], i.e.,

$$p = k\frac{E\mu_\alpha \beta v^n}{C_p r^m R^l} \tag{1}$$

where k is the proportion coefficient. E is the energy of pulsed laser. μ_α is the optical absorption coefficient of the sample. R is the radius of photoacoustic source. r is the distance between the ultrasonic transducer and the photoacoustic source. In Eq. (1), n, m, and l are constants: $0.5 < n < 2$, $0 < m < 1$, and $0 < l < 2$. From Eq. (1), it can be seen that the intensity of the photoacoustic signal (p) is related to the parameters of the laser and ultrasonic transducer (E, r and R), optical properties (μ_α), and thermal and ultrasonic properties (β/C_p, and v). For the different types of blood, the optical, ultrasonic and thermal properties are different, which results in a difference in the photoacoustic signal. Then, the different types of blood can be distinguished via the inversion and analysis of the photoacoustic signal.

2.2. WNN

In this work, the WNN algorithm [21] was used to classify and discriminate real and fake blood because it combines the wavelet transform and the artificial neural network. It has the great capacities of strong learning, self-adaptability and fault tolerance because it avoids nonlinear optimization problems, including the blindness of structure design and local optimization of BPNN [22]. The basic structure of WNN is shown in Fig. 1.

In Fig. 1, the WNN has three layers, i.e., input layer (Layer 1), hidden layer (Layer 2), and output layer (Layer 3). Suppose that the input layer has m ($m = 1, 2,\ldots,M$) neurons, and the p groups of input photoacoustic PPVs are expressed as x_m^p. The hidden layer has k ($k = 1,2,\ldots.K$) neurons. The output layer has n ($n = 1,2,\ldots,N$) neurons.

In the hidden layer, a neuron excitation function $h_k(x)$, i.e., a Morlet-liked wavelet basis function, was constructed based on the Morlet wavelet basis [23] to replace the sigmoid function. The Morlet-liked wavelet is given as follows:

$$h_k(x) = \exp(-x^2/2)\cdot\cos(1.75x) \tag{2}$$

The output values of the hidden layer (O_k^p) can be expressed as follows:

$$O_k^p = h_k\left(\frac{\sum_{m=1}^{M}\omega_{km}x_m^p - b_k}{a_k}\right) \tag{3}$$

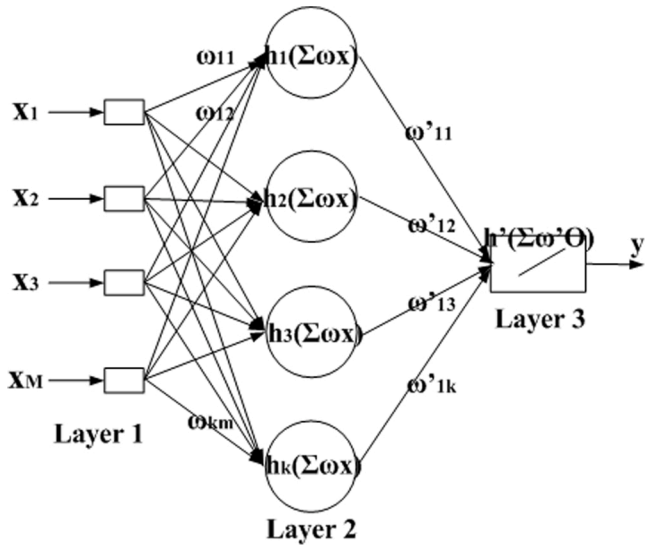

Fig. 1. The basic structure of WNN.

where ω_{km} is the weight value between the input layer and the hidden layer and b_k and a_k are the translation factor and scaling factor of the wavelet basis function $h_k(x)$, respectively. m and k are the neuron nodes in the input layer and the hidden layer, respectively.

The output values of output layer y_n^p can be expressed as follows:

$$y_n^p = h'\left(\sum_{k=1}^{K} \omega'_{nk} O_m^p\right) \tag{4}$$

where ω'_{nk} is the weight value between the hidden layer and the output layer. In the output layer, the linear function was chosen as the excitation function $h'(\cdot)$.

In the WNN, the real output values $y(n)$ are denoted as $y(n) = y_n^p$. Suppose that the desired output values of WNN are denoted as d_n^p, and the objective error function of training can be expressed as follows:

$$E_n^p = \sum_{p=1}^{P} E^p = \frac{1}{2P} \sum_{p=1}^{P} \sum_{n=1}^{N} (d_n^p - y_n^p) \tag{5}$$

In addition, error back propagation was used to correct the parameters of the WNN network, i.e., the weights (ω_{km} and ω_{nk}), translation factor and scaling factor (b_k and a_k) of the wavelet basis function, which are expressed as follows:

$$\begin{cases} \omega_{nk}^{new} = \omega_{nk}^{old} + \eta \sum_{k=1}^{K} \dfrac{\partial E_n^p}{\partial \omega_{nk}} \\ \omega_{km}^{new} = \omega_{km}^{old} + \eta \sum_{m=1}^{P} \dfrac{\partial E_n^p}{\partial \omega_{km}} \\ a_k^{new} = a_k^{old} + \lambda \sum_{m=1}^{P} \dfrac{\partial E_n^p}{\partial a_k} \\ b_k^{new} = b_k^{old} + \lambda \sum_{m=1}^{P} \dfrac{\partial E_n^p}{\partial b_k} \end{cases} \tag{6}$$

where ω_{nk}^{new}, ω_{km}^{new}, a_k^{new} and b_k^{new} are the corrected weights, translation and scaling factors of the wavelet basis function, respectively. ω_{nk}^{old}, ω_{km}^{old}, a_k^{old} and b_k^{old} are the uncorrected weights, translation and scaling factors of the wavelet basis function, respectively. η and λ are the learning rate factors.

2.3. PSO

The PSO [24] algorithm is a kind of evolutionary computation technology that originates from research on the predation behavior of birds. The basic mechanism of PSO is to find the optimal solution through cooperation and information sharing among individuals in the population. In this work, to improve the classification and discrimination rate of real and fake blood, the parameters of the WNN network, including weights, thresholds, translation factor and scaling factor of the Morlet-liked wavelet basis function, were optimized by the PSO algorithm. The basic flow chart of the PSO algorithm is shown in Fig. 2.

In the PSO algorithm, the velocity and location vectors of the particles are the two most important properties, which can be updated via the following relationship:

$$\begin{cases} \nu_i(n+1)^{k+1} = \omega \cdot \nu_i(n)^k + c_1 \cdot r_1 \cdot (P_i^k - x_i(n)^k) + c_2 \cdot r_2 \cdot (G_i^k - x_i(n)^k) \\ x_i(n+1)^{k+1} = x_i(n)^k + \nu_i(n+1)^{k+1} \end{cases} \tag{7}$$

where $\nu_i(n)$ is the initial velocity of the i^{th} particle, $i = 1,2,\ldots,M$, and M is the total number of particles. $\nu_i(n+1)$ is the updated velocity of the i^{th} particle, ω is the inertia weight, and $\omega \in [0,1]$. c_1 and c_2 are the acceleration factors, r_1 and r_2 are random numbers uniformly distributed in (0, 1), $x_i(n)$ is the initial location of particle, $x_i(n+1)$ is the updated location of particle, P_i is the previous best particles, i.e., the individual best location of the i^{th} particle, G_i is the global best particle, i.e., the global best location among all the particles. k is the iteration index. According to the Eq. (7), the updated particles are brought into the WNN network again, then the new individual and population extremum can be obtained via the training and test operations, and the worst particles are replaced by the best ones according to the migration strategy.

In addition, the inertia weight ω is related to the global and local search capabilities of the PSO algorithm. With the increase in inertia weight, the global search capability can be improved, but the local search capability is weakened. Conversely, the global search capability can be weakened, but the local search capability is improved. To balance the two search capabilities, the inertia weight can be adjusted by the linear decreasing inertia weight (LDIW) strategy [25], i.e.,

$$w(k) = w_{start} - (w_{start} - w_{end}) \times (k/T_{\max}) \tag{8}$$

where k is the present number of iterations, $T_{\max}$ is the maximum number of iterations, w_{start} is the initial inertia weight, and w_{end} is the final inertia weight at the maximum number of iterations. $w(k)$ is inertia weight variant, $w(k) \in [0,1]$. In general, at the minimum number of iterations, the inertia weight $w(k)$ is at a maximum, and the global search capability is the best. Then, $w(k)$ gradually decreases with increasing number of iterations.

3. Experimental

3.1. Set-up

In this work, a set of photoacoustic detection system of blood was established, which is shown in Fig. 3.

In the system, a tunable Nd:YAG 532 nm pumped OPO pulsed laser (OPOletteTM, 532 II, OPOTEK Inc., USA) was used as the excitation source, its repetition rate was 20 Hz, the duration time was 7 ns, and the maximum output energy of the unit pulse was approximately 2 mJ. A focused ultrasonic transducer (Doppler Co., China) with a central echo frequency of 2.5 MHz was used to capture the photoacoustic signal of the blood. Then, the photoacoustic signal was amplified by a signal amplifier (ATA-5620, Aigtek Co. China) with a gain of 60 dB and filtered via a low-pass filter (BLP-7-75+, Mini-Circuits, USA). After that, a two-channel digital oscilloscope (54642D, Agilent Co., USA) with a bandwidth of 500 MHz and acquisition rate of 2 Gs/s was used to acquire and display the photoacoustic signal. Finally, a GPIB-USB card (GPIB-USB-

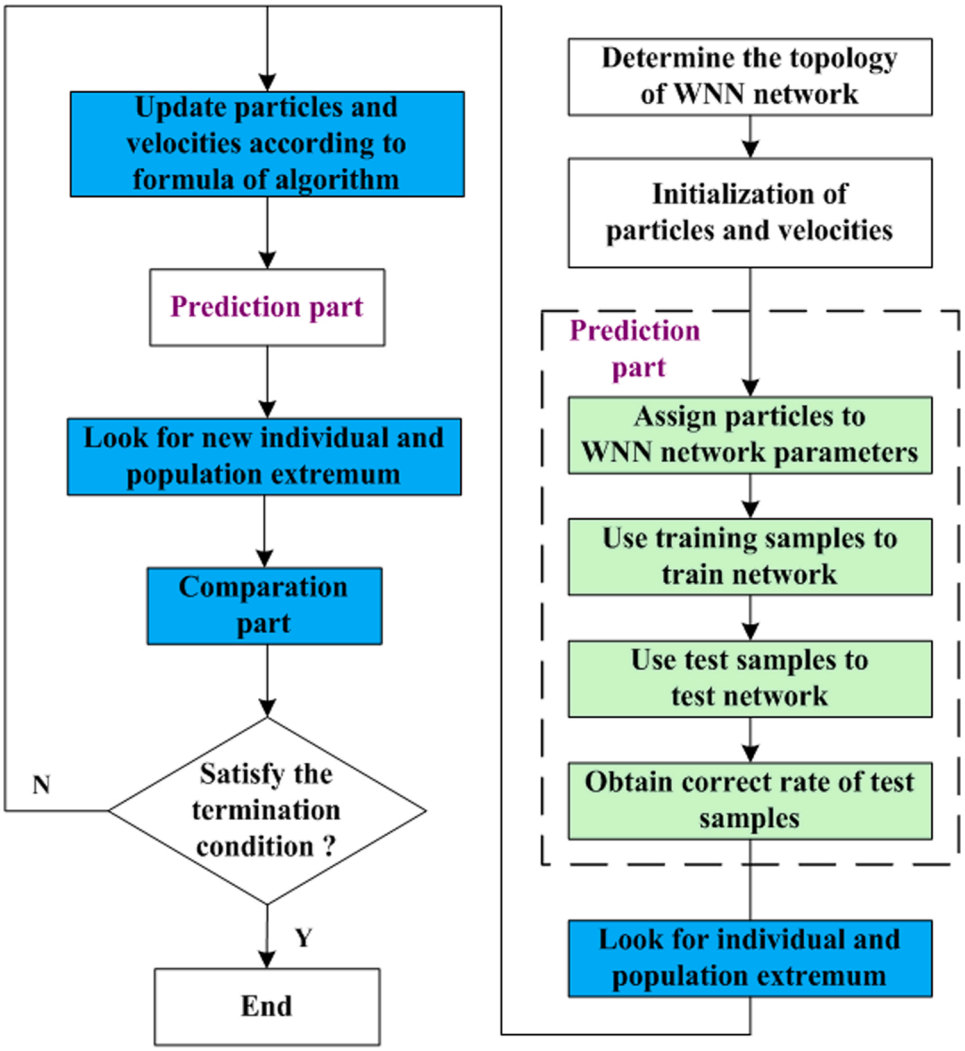

Fig. 2. Flow chart of PSO algorithm.

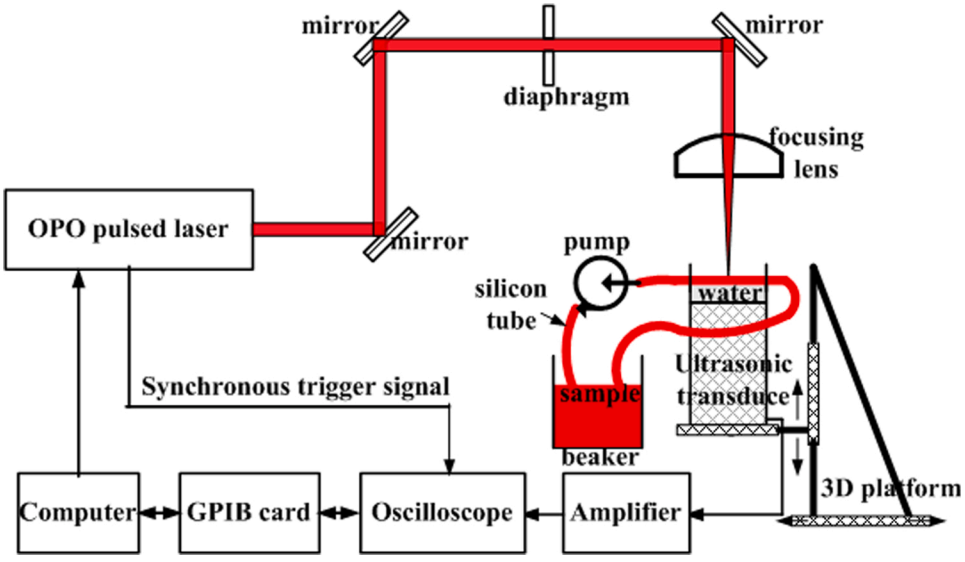

Fig. 3. Experimental set-up.

HS, NI Co., USA) was used to transmit the photoacoustic data of blood into the computer. The signal acquisition and data storage operations were performed via a self-developed program based on the LabVIEW software platform. In addition, to facilitate the replacement of blood samples in the experiments, a set of circulation sub-system of blood samples was built, which consisted of mini pump, transparent silicon tube (inner and outer diameters were 3 mm and 5 mm), and beakers. The irradiated section of the silicon tube runs through and was fixed on the walls of a plastic cylinder, which was placed in front of the head face of the ultrasonic transducer. The distance between the lower edge of the outer wall of the silicon tube and the surface of the ultrasonic transducer is approximately 5.5 mm. In the experiments, water was used as the coupling agent, and it was loaded between the silicon tube and the ultrasonic transducer. To ensure that the focused laser spot precisely falls into the blood sample loaded in a silicon tube, the laser spot location can be adjusted via a 3D translational platform. Before the experiments, the OPO pulsed laser was preheated for approximately 30 min. During the experiments, the room temperature was kept at approximately 20 °C.

In this work, a focused ultrasonic transducer with a central echo frequency of 2.5 MHz was used to capture the photoacoustic signal of blood samples. The echo signal and frequency spectrum of the ultrasonic transducer are shown in Fig. 4(a) and (b), respectively. From Fig. 4(a), it can be seen that the echo signal profile of the ultrasonic transducer looks like a bipolar sinusoidal wave. From Fig. 4(b), we can see that the central echo frequency of the ultrasonic transducer is approximately 2.5 MHz. Fig. 4(c) shows the Hilbert transform and Hilbert envelope of the photoacoustic echo signal for the ultrasonic transducer. According to reference [26], the axial resolution of the ultrasonic transducer can be obtained by using the full width at half-maximum (FWHM) of the Hilbert-transformed envelope of the time-domain photoacoustic signal. Fig. 4(c) shows that the axial resolution of the ultrasonic transducer is approximately 375 μm. Although the axial resolution is relatively larger than the size of red blood cells (approximately 2–8 μm), the inner diameter (3 mm) of the silicon tube is sufficiently large to ensure that the focused laser spot falls into the blood sample in the silicon tube and generates the effective photoacoustic signal of blood.

3.2. Blood samples

In the experiments, four kinds of animal blood (horse, cow, rabbit, and sheep) were supplied by Zhengzhou Yikang Bioengineering Co., Ltd., and two kinds of fake blood (props blood and red ink) were used as experimental samples, which are shown in Fig. 5. Prop blood is fake blood used for stage or movie performances and was purchased from Manxiang e-commerce Co., Ltd. (Yiwu, China). The main components of prop blood are edible pigment, honey and water. Red ink was purchased from Cheng Zhutang Co., Ltd. (Jiangxi, China). The main components of red ink are natural mineral pigments, gum, spices, and water. Although the colour of props blood and red ink looks like the real blood, there is no haemoglobin, haemocytes, or other blood components in either of them. To prevent animal blood from clotting, anticoagulant (ethylenediamine tetraacetic acid, EDTA) at a proportion of 1.6 mg/mL was added to the animal blood samples. The total number of blood samples was 150 groups, that is, the number of each kind of blood sample was 25 groups, where the training samples were 20 groups and the test samples were 5 groups. In all experiments, we used medical alcohol to sterilize the beaker and silicon tube in the circulation sub-system and then boiled them in water for a secondary disinfection.

3.3. Experimental results and analysis

In experiments, 10-mL blood samples were loaded into the circulation sub-system. The excitation wavelengths of the OPO pulsed laser from 700 nm to 1064 nm with an interval of 5 nm were considered. The time-resolved photoacoustic signals of all blood samples at different excitation wavelengths were obtained an average of 128 times. Fig. 6 (a–d) shows the time-resolved photoacoustic signals of the six kinds of blood samples at 750 nm, 780 nm, 905 nm, and 1000 nm, respectively.

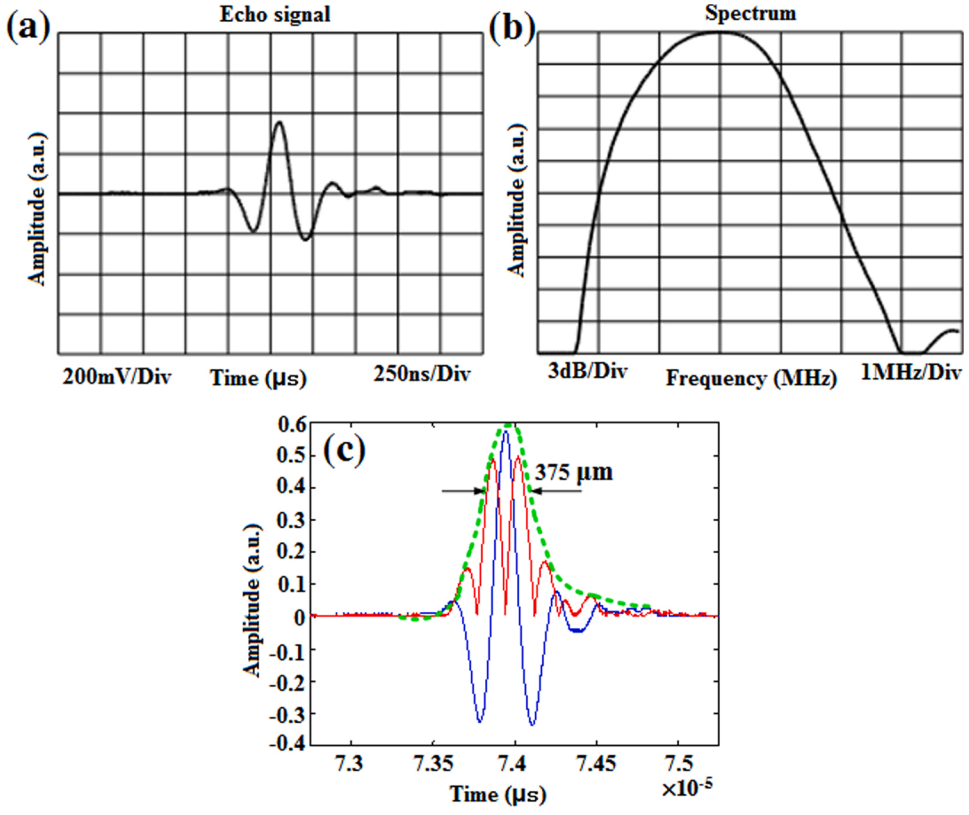

Fig. 4. (a) Time-domain echo signal, (b) the frequency spectrum, and (c) the axial resolution of the ultrasonic transducer.

Fig. 5. Experimental blood samples. (a) horse blood; (b)cow blood; (c)rabbit blood; (d)sheep blood; (e)props blood; (f)red ink.

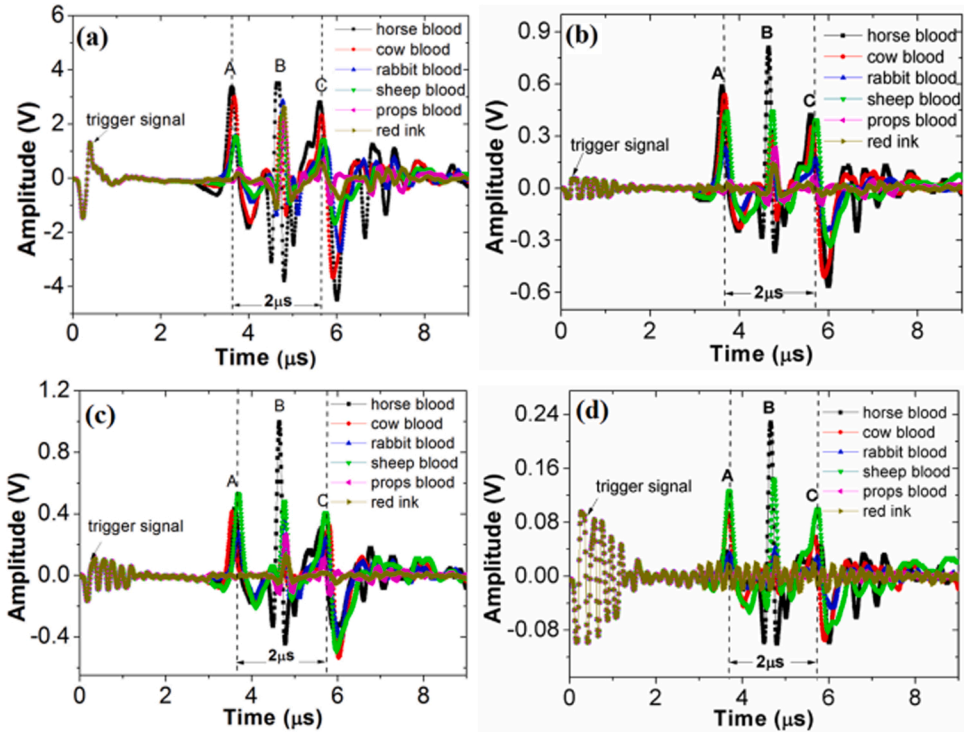

Fig. 6. Time-resolved photoacoustic signals of six different kinds of blood samples at the excitation wavelengths of 750 nm (a), 780 nm (b), 905 nm (c), and 1000 nm (d).

Fig. 6(a–d) shows that the different kinds of blood samples have different amplitudes and profiles of time-resolved photoacoustic signals at a certain wavelength. In general, the amplitudes of real blood samples are larger than those of fake blood samples. Especially for horse blood, its amplitudes are the largest among the blood samples. Moreover, three obvious peak signals (labeled with A, B, and C in Fig. 6(a–d)) exist in the time-resolved photoacoustic signal of the real blood samples. The arrival times of the three peaks are approximately 3.7 μs, 4.7 μs, and 5.7 μs, respectively. However, for the photoacoustic signal of the two kinds of fake blood, only one peak signal at approximately 4.7 μs is relatively large, but the two others are not obvious. In Fig. 6(a–d), according to the edge effect of the photoacoustic signal of the absorbers [27], we know that the first peak (i.e., A) is the photoacoustic signal for the beginning (first edge) of the inner diameter of the silicon tube. Since the silicon tube was immersed in the coupling water, supposing that the sound speed in water is approximately 1500 m/s, we can compute the theoretical distance between the surface of the ultrasonic transducer and the beginning of the inner diameter of the silicon tube as approximately 5.55 mm, which is basically in agreement with the actual distance (5.5 mm). From Fig. 6, it can be seen that the arrival time of peak signal C is approximately 5.7 μs. The time difference between A and C is approximately 2 μs. From the results, we know that the distance between peak A and peak C is approximately 3 mm based on the sound speed of 1500 m/s in the blood, which is in good agreement with the actual inner diameter of the silicon tube. Therefore, the third peak (i.e., C) is the photoacoustic signal for the upper edge of the inner diameter of the silicon tube, i.e., peak C corresponds to the end (second edge) of the inner diameter of the silicon tube. Then, we found that the second peak (i.e., B) was the photoacoustic signal of the focused laser spot in the blood. From the arrival time of the second peak, it can be seen that the focused spot of the laser lies in the middle of the silicon tube, and the parts between point A and point C are the time-resolved photoacoustic signals of blood samples. In addition, Fig. 6(a–d) shows that the arrival time of the second peak (i.e., B) of different blood samples is different. The arrival times of the peak points of real blood samples are slightly less than those of the fake ones, which demonstrates that the ultrasonic velocities of real blood samples are larger than those of the fake ones. For three kinds of real blood, the arrival time of the peak point of horse blood is less than those of the two others, and the time order from small to large is horse blood, cow blood and rabbit blood. For the two kinds of

fake blood, the time of peak point of red ink is slightly less than that of the props blood. In addition, Fig. 6(a–d) shows that the amplitudes of the time-resolved photoacoustic signals of six different kinds of blood samples are different at different wavelengths, although their profiles are similar. At the same time, the amplitudes are also different between real blood and fake blood at different wavelengths. In Fig. 6(a–d), the amplitudes of the time-resolved photoacoustic signal of blood samples at 750 nm are larger than those of other wavelengths. Moreover, at a wavelength of 750 nm, the amplitudes of all blood samples, i.e., the amplitudes of the second peak (i.e., B) shown in Fig. 6, are large, and the amplitude differences between real blood and fake blood are relatively small. However, at wavelengths of 780 nm, 905 and 1000 nm, the amplitude differences are large between real blood and fake blood, i.e., the amplitudes of real blood are relatively larger than those of fake blood, especially for horse blood and sheep blood.

According to Eq. (1), the amplitudes of the photoacoustic signal are related to the absorption coefficients of the samples. To compare the different optical absorption rates between real blood and fake blood at different wavelengths, photoacoustic PPVs were used in this work. The photoacoustic PPVs of all samples at full wavelengths (700−1064 nm) were obtained according to the time-resolved photoacoustic signal of blood samples from 3.7 μs to 5.7 μs. For six different kinds of real and fake blood samples, since the large amount of data cannot be completely shown here, the photoacoustic mean peak-to-peak spectra were obtained based on the photoacoustic PPVs of all samples at 700−1064 nm, which are shown in Fig. 7. According to the relationship between the photoacoustic amplitude and the optical absorption, we know that the photoacoustic PPV spectra given in Fig. 7 are a representation of the optical absorption spectra of the samples. From Fig. 7, it can be seen that not only are the optical absorption of blood samples different at the different wavelengths but also the optical absorption between the real blood and the fake blood samples are also different at the same wavelength. At full wavelengths, the PPVs of all blood samples at wavelengths of 700−850 nm were obviously larger than those at wavelengths of 850−1064 nm. At the same time, at 700−850 nm, the photoacoustic PPVs of real blood samples are larger than those of fake samples, especially at 700−760 nm. At 850−1064 nm, the differences in PPVs between the real blood samples and the fake samples are not obvious except near the wavelengths of 905 nm, 950 nm, and 1000 nm. However, we also find that some PPVs of real and fake blood samples overlap at some wavelengths, which results in the difficulty of distinguishing real and fake blood from the time-resolved photoacoustic signal and peak-to-peak spectra.

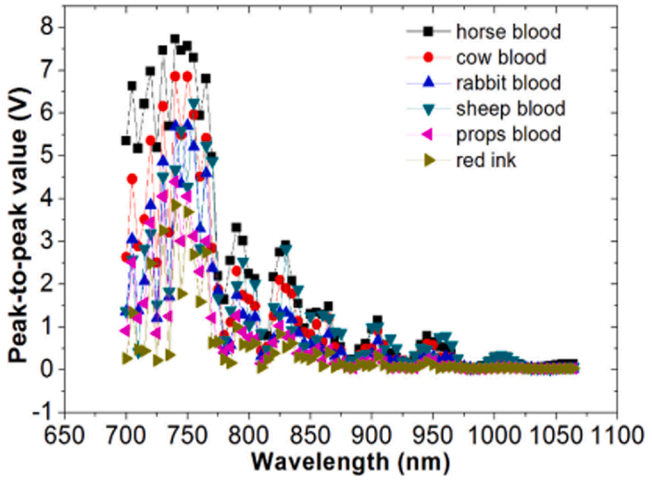

Fig. 7. Photoacoustic mean peak-to-peak spectra of blood samples.

4. Classification and discrimination of real and fake blood

4.1. Classification and discrimination results based on WNN and WNN-PSO

To ensure the accurate classification and discrimination of real and fake blood, the WNN algorithm (see Fig. 1) was used in this work. Six different kinds of blood samples with 150 groups were used, where 120 groups were used as the training samples and 30 groups were used as the test samples. The photoacoustic PPVs of blood samples at full wavelengths were used as the input data of the WNN network, i.e., the neuron number of the input layer was 74. The neuron number in the hidden layer was determined by using the empirical formula [28], i.e., $\sqrt{m+n}+a$, where m is the neuron number in the input layer and n is the number of neurons in the output layer, i.e., 1. In general, a is a constant, $a \in [0, 10]$. Therefore, the number of neurons in the hidden layer can be chosen in the interval $[8, 18]$. For the training operation of the WNN network, the supervised training method was used, i.e., 1, 2, 3, 4, 5, and 6 were used to label horse blood, cow blood, rabbit blood, sheep blood, props blood, and red ink, respectively. In addition, to improve the classification and discrimination rate of real and fake blood, the weights, thresholds, translation and scaling factor of the Morlet-liked wavelet basis function (see Eq. (2)) of the WNN network was optimized by the PSO algorithm. To obtain the optimal number of neurons in the hidden layer from 8 to 18, under two optimal learning rate factors (see Eq. (6)), i.e., η =0.001 and λ =0.1, the effect of the number of neurons in the hidden layer on the correct rates of classification and discrimination of real and fake blood based on the WNN algorithm and WNN-PSO algorithm were obtained and compared, which is shown in Fig. 8(a).

In Fig. 8(a), for the WNN algorithm, the largest correct rate is 56.7 % when the number of neurons in the hidden layer is 8. However, for the WNN-PSO algorithm, the correct rates under different numbers of neurons in the hidden layer are all improved. When the number of neurons in the hidden layer for the WNN-PSO algorithm is 10 and 13, the correct rate can reach 93.3 %. To obtain the optimal number of neurons in the hidden layer, the mean square error curves of 10 and 13 neurons in the training process were obtained, which are shown in Fig. 8(b). In Fig. 8 (b), the mean square errors of the neuron number of 13 in the hidden layer are less than those of the neuron number of 10. Therefore, the neuron number of 13 in the hidden layer was chosen in this work.

Then, the effects of learning rate factors (η, and λ) on the correct rates were investigated for both algorithms, as shown in Fig. 8(c) and (e), respectively. The range of the learning rate factor η is from 0.001 to 0.01, and the range of the learning rate factor λ is from 0.1 to 1. In Fig. 8(c), when the learning rate factor η is 0.001, the correct rate based on the WNN algorithm is the largest, i.e., 56.7 %. For the WNN-PSO algorithm, the largest correct rate is 93.3 % when the learning rate factor η is 0.001 and 0.002. Moreover, with increasing learning rate factor η, the correct rates of both algorithms all decrease. To obtain the optimal value of the learning rate factor η, the mean square error curves for the learning rate factor η =0.001 and 0.002 were obtained, which are shown in Fig. 8(d). From Fig. 8(d), it can be found that the mean square errors of η=0.001 are less than those of η =0.002. Therefore, the learning rate factorη=0.001 was determined as the optimal value of η. For another learning rate factor λ, Fig. 8(e) shows that with the increase in the learning rate factor λ, the correct rate of the WNN algorithm first increases and then decreases. When the learning rate factor λ is 0.08, the correct rate of the WNN algorithm is the largest, i.e., 63.3 %. However, for the WNN-PSO algorithm, the correct rate first increases, then decreases and finally increases. When the learning rate factor λ is 0.05 and 0.1, the correct rates of the WNN-PSO algorithm are the largest, i.e., 96.7 %. To determine the optimal learning rate factor λ, Fig. 8(f) gives the mean square error curves of λ =0.05 and 0.1 with increasing training times. In Fig. 8(f), both mean square error curves decrease with increasing training time. The mean square errors of λ =0.1 are less than

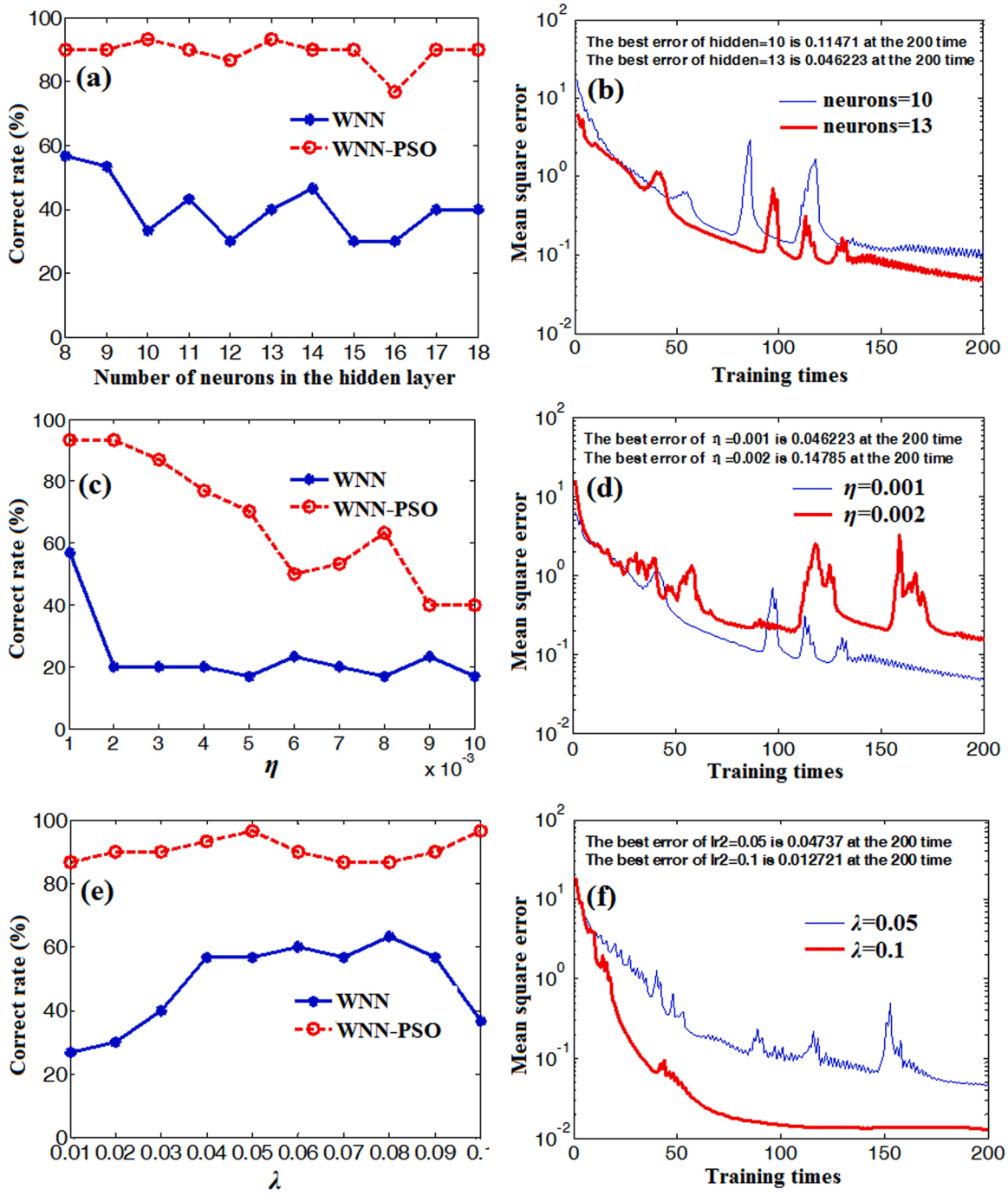

Fig. 8. The effect of parameters of WNN network on the correct rates of classification and discrimination of real and fake blood. (a) the effect of neurons number of hidden layer; (b) the mean square error curves of two different neurons number of hidden layer in the training process;(c) the effect of learning factor η; (d) the mean square error curves of two different values of learning factor η;(e) the effect of learning factor λ; (f) the mean square error curves of the learning factor.

those of λ =0.05. Therefore, the learning rate factor λ =0.1 is optimal. From Fig. 8(a)-(f), it can be seen that the correct rate of classification and discrimination of real and fake blood based on the WNN-PSO algorithm is superior to that of the WNN algorithm.

Then, for the WNN-PSO algorithm, the effects of the inertia weight (w) on the correct rate were studied, which are shown in Fig. 9(a)–(d).

In Fig. 9(a), when the two acceleration coefficients (c_1 and c_2) are set to 1.8 and 1.3, the inertia weight (w) is set to different constants, and the effect of inertia weight on the correct rates of classification and discrimination of real and fake blood are obtained. From Fig. 9(a), it can be seen that when w is 0.4, the correct rate is the lowest, i.e., 76.7 %. When w is 0.6 and 0.7, the correct rates can reach the maximum value, i.e., 93.3 %. However, from the mean square error curves in the training process shown in Fig. 9(b), we can find that the mean square errors of w =0.7 are less than those of w =0.6.

In this work, to balance the local and global search capabilities of the PSO algorithm, the inertia weight (w) was adjusted by using the LDIW strategy (see Eq. (8)). Here, the maximum number of iterations ($T_{\max}$) was set to 200, and the initial inertia weight (w_{start}) was set to 1. The dynamic range of inertia weight (w) corresponding to the final inertia weight (w_{end}) is shown in Table 1.

The effect of w_{end} on the correct rates based on the WNN-PSO algorithm is shown in Fig. 9(c). In Fig. 9(c), the correct rate can reach the maximum value when w_{end} is 0.3 and 0.7. From Table 1, we know that

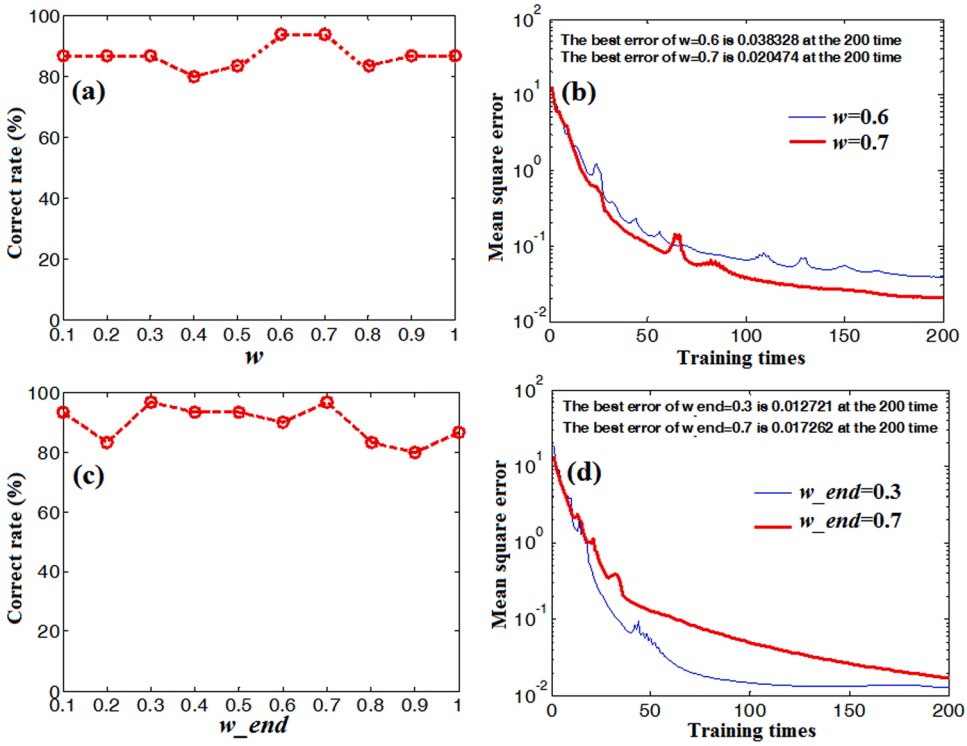

Fig. 9. Effects of PSO parameters on the correction rates of classification and discrimination of real and fake blood samples based on WNN-PSO algorithm. (a) the effect of inertia weight w; (b) mean square error curves of two different inertia weights; (c) the effect of the final inertia weight w_{end}; (d) mean square error curves of two different values of final inertia weight.

Table 1
The dynamic range of inertia weight (w) corresponding to the final inertia weight (w_{end}).

w_{end}	0.1	0.2	0.3	0.4	0.5	0.6	0.7	0.8	0.9	1.0
w	1→0.1	1→0.2	1→0.3	1→0.4	1→0.5	1→0.6	1→0.7	1→0.8	1→0.9	1.0

for w_{end} =0.3, the corresponding dynamic decreasing range of w is from 1 to 0.3. For w_{end} =0.7, the dynamic decreasing range of w is from 1 to 0.7. To obtain the optimal value of w_{end}, the mean square error curves in the training process of both values of w_{end} are obtained, which are shown in Fig. 9(d). In Fig. 9(d), the mean square errors of w_{end} =0.3 are less than those of w_{end} =0.7. Therefore, w_{end} =0.3 is optimal. In addition, compared with Fig. 9(a), for the fixed value of inertia weight, i.e., w =0.7, the global search capability of the PSO algorithm is always stronger than that of the local search capability. Although the convergence speed of the PSO algorithm is faster, the correct rate is not satisfactory. However, for the dynamic inertia weight based on the LDIW strategy, when w_{start} is 1 and w_{end} is 0.3, the inertia weight (w) can be changed in the range of 1 to 0.3. At the beginning of the PSO algorithm iteration, a larger inertia weight can ensure the search of a larger area and locate the optimal solution quickly. Then, with the decrease in the inertia weight, the local search capability is stronger than that of the global search capability, which results in a more accurate solution, although the number of iterations is increased. From Fig. 9(a) and (c), it can be seen that the correct rate is improved from 93.3% to 96.7% by using the LDIW strategy. In addition, the prediction results of the inertia weight w =0.7 and the final inertia weight w_{end} =0.3 for 120 groups of training blood samples are compared, which are shown in Fig. 10. From Fig. 10, it can be seen that the correct rate of the final inertia weight w_{end} =0.3 for the training samples is 99.2 %, which is better than that of the inertia weight w =0.7.

In the PSO algorithm, the two acceleration factors (c_1 and c_2) have an important role in the search capability of the optimal solution and convergence speed of the PSO algorithm. The effects of the two acceleration factors (c_1 and c_2) on the correct rate were studied. Since a mutual relationship exists between the different values of c_1 and c_2, one of two acceleration factors should be determined first. In this work, the optimal value of the acceleration factor (c_2) was determined first. In the standard PSO algorithm, the values of c_1 and c_2 are usually c_1=c_2 = 2 [29], and another commonly used value is c_1=c_2 = 1.49445 [30]. In

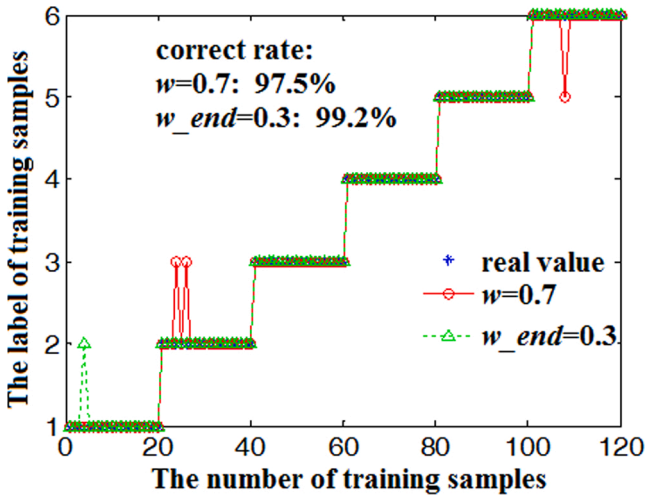

Fig. 10. Prediction results of inertia weight w and final inertia weight w_{end} for train blood samples.

addition, Carlisle [31] integrated various research results in PSO parameter selection and analyzed the influence of different control parameters on algorithm performance in detail. He proposed a group of relatively perfect and reasonable parameter values, $c_1 = 2.8$ and $c_2 = 1.3$ [32]. However, when it is applied in the classification and discrimination of real and fake blood in this manuscript, it does not ensure whether these values are still appropriate or not, and what the training error, convergence speed and accuracy are. Consequently, to solve this problem, the above three groups of parameters were selected as the initial values, and then our experiments were conducted under different values of c_1. The range of c_1 was set from 1 to 2 with an interval of 0.1. The effects of different values of c_1 on the correct rate under three values of c_2 were studied, which are shown in Fig. 11(b). At the same time, the correct rates of different coupling values of c_1 and c_2 are obtained and compared, shown in Fig. 11(b).

From Fig. 11(a–b), it can be seen that the correct rate of $c_2 = 1.3$ is the largest. Therefore, $c_2 = 1.3$ was first set as the optimal parameter value of c_2. Then, we determine the optimal acceleration factor of c_1 from Fig. 11(a). In Fig. 11(a), we can find that the correct rates are the highest for c_1 =1.7 and 1.8 when $c_2 = 1.3$. To compare the results between c_1 =1.7 and 1.8, the effect of training times on the correct rate was obtained, which is shown in Fig. 11(c). From Fig. 11(c), it can be seen

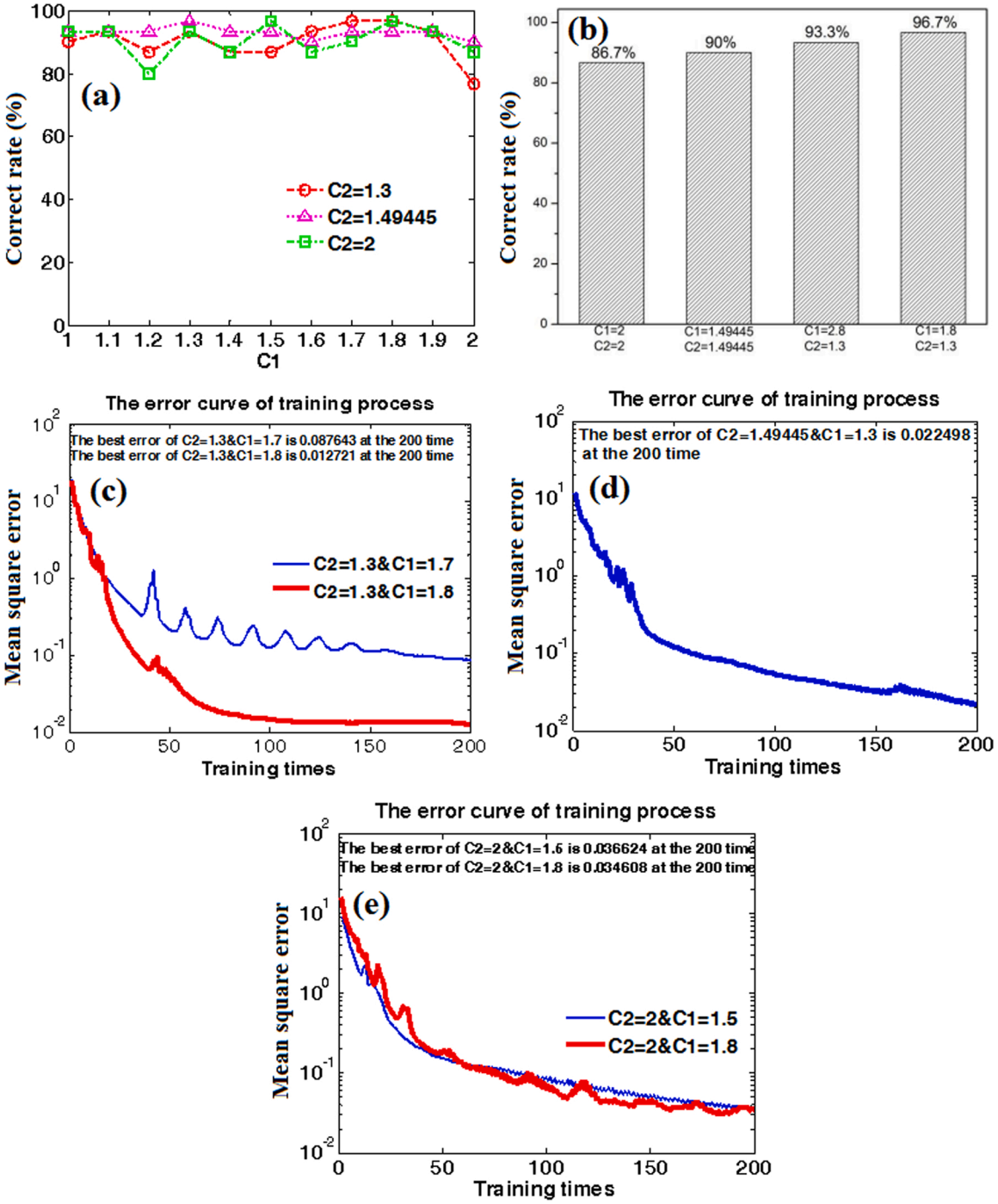

Fig. 11. (a)The influence of c_1 on the correct rate of classification and discrimination of real and fake blood; (b) the effect of different values of c_1 on the correct rate under three values of c_2; (c) the effect of the training times on the mean square error under c_2=1.3; (d) the effect of the training times on the mean square error under c_2=1.49445; (e) the effect of the training times on the mean square error under c_2=2.

that the effect of c_1 =1.8 is the best because its minimum training error is less than approximately 0.0127. To compare the effect of c_1 =1.8, and c_2 = 1.3, the correct rates of four different coupling values of c_1 and c_2 were obtained, which are shown in Fig. 11(b). From Fig. 11(b), it can be seen that when c_1 =1.8 and c_2 = 1.3, the correct rate is the largest (i.e., 96.7 %). To further ensure the effect of c_1 =1.8, and c_2 = 1.3, the effect of training times on the mean square error under different coupling values of c_1 and c_2 was studied. When c_1 = 1.3 and c_2 = 1.49445, the effect of training times on the mean square error was also obtained, as shown in Fig. 11(d). From Fig. 11(d), it can be seen that the mean square error is approximately 0.0225, which is larger than that of c_1 =1.8, and c_2 = 1.3. When c_2 = 2, c_1 =1.5, and 1.8, the effects of training times on the mean square error were also obtained, which are shown in Fig. 11(e). From Fig. 11(e), it can be seen that the mean square errors are 0.0366 and 0.0346, respectively, which are all larger than those of c_1 =1.8, and c_2 = 1.3. Therefore, for w, c_1, and c_2 in the PSO algorithm, when w dynamically changes in the range from 1 to 0.3, c_1 is 1.8, and c_2 is 1.3, the results are satisfied.

Fig. 12(a) shows the effect of the number of iterations on the correct rate based on the WNN and WNN-PSO algorithms. From Fig. 12(a), it can be seen that for the WNN-PSO algorithm, the correct rate increases with increasing iteration times. When the number of iterations is 1, the correct rate is only 60 % and is less than that of the WNN algorithm (i.e., 63.3 %). With the increase in the iteration times, the correct rate is over 70 % and is larger than that of the WNN algorithm. Then, with the continuous increase in the iteration times, the correct rate is also continuously improved. When the number of iterations is 126, the correct rate of the WNN-PSO algorithm reaches a maximum, i.e., 96.7 %. After that, with the continuous increase in the iteration times, the correct rate of the WNN-PSO algorithm is still constant.

Then, the effect of the training times of both algorithms on the mean square errors was also studied, which are shown in Fig. 12(b). In Fig. 12 (b), with the increase in the training times, although the mean square errors of both algorithms all decrease with an exponential function, the mean square errors of the WNN-PSO algorithm are less than those of the WNN algorithm. Moreover, at the beginning of training, the oscillation phenomenon of the mean square error is greatly reduced via the WNN-PSO algorithm. From Fig. 12(b), it can be seen that the best mean square error of the WNN-PSO algorithm is approximately 0.012721 at the training times of 200, which is obviously less than that of the WNN algorithm, i.e., 0.21281.

To further compare the performance of the WNN algorithm and WNN-PSO algorithm, the results of classification and discrimination for test blood samples were obtained, which are shown in Fig. 12(c). From Fig. 12(c), it can be found that the correct rate of the WNN algorithm for the test blood samples is not satisfactory, i.e., 63.3 %. Especially for the first kind of real blood sample, i.e., the five horse blood samples, the prediction result of only one sample is correct. For other kinds of blood samples, one or two prediction errors also occur. However, for the WNN-PSO algorithm, only one sheep blood sample was misjudged as cow blood, and the correct rate reached 96.7 %, which was much larger than that of the WNN algorithm.

4.2. *Classification and discrimination results based on PCA-WNN-PSO*

In Section 4.1, the photoacoustic PPVs of blood samples at full wavelengths (700−1064 nm) were used as the input values. However, from Fig. 7, we know that there is obvious overlap in the photoacoustic peak-to-peak spectra. Moreover, at 850−1064 nm, the differences in PPVs were not obvious between real and fake blood samples. Therefore, the photoacoustic peak-to-peak spectra at full wavelengths not only contain the useful characteristics of blood, but also involve some useless information limited to distinguishing real and fake blood. At the same time, too many parameters, high computational complexity, and the large dimension of input data also greatly impact the classification and discrimination of real and fake blood. To further improve the correct rate of the classification and discrimination for real and fake blood based on the WNN-PSO algorithm, the PCA algorithm [33] was used to extract

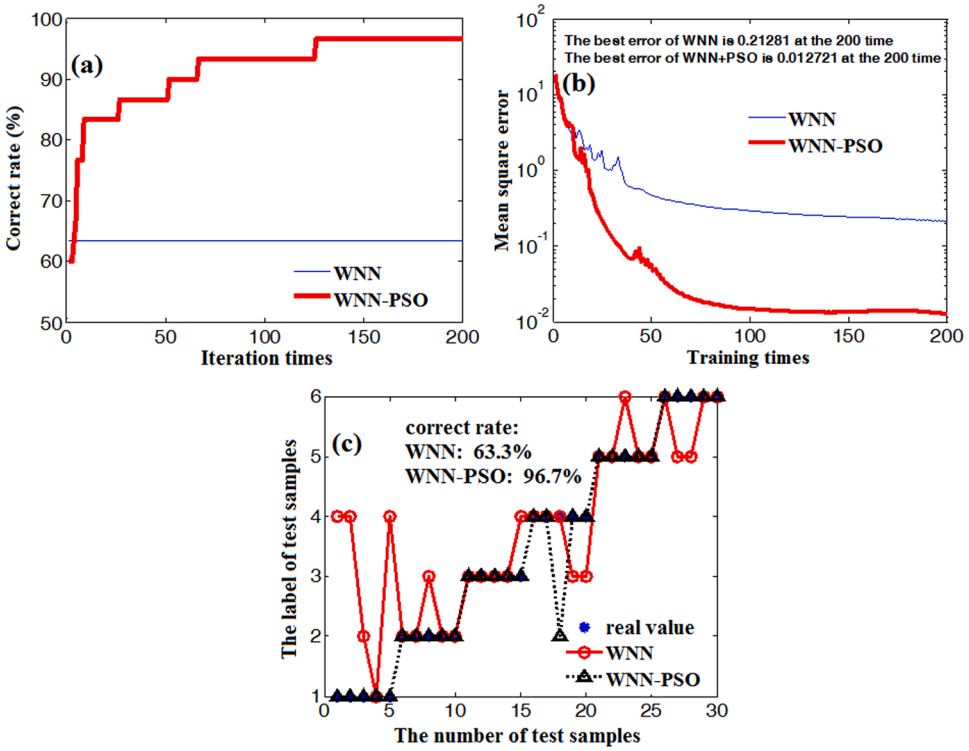

Fig. 12. Comparison results of classification and discrimination of real and fake blood based on WNN algorithm and WNN-PSO algorithm. (a) the effect of iteration times of WNN-PSO algorithm on the correct rate; (b) the effect of training times of both algorithms on the mean square error; (c) comparison results of classification and discrimination for test samples between WNN algorithm and WNN-PSO algorithm.

the feature information from the photoacoustic peak-to-peak spectra.

The basic theory of the PCA algorithm is data dimension reduction, that is, the information of many variables is replaced by less variable information, but most of the original information is preserved to the greatest extent. The PCA algorithm can be described as follows,

$$\begin{cases} Z_1 = k_{11}x_1 + k_{12}x_2 + \ldots + k_{1p}x_p \\ Z_2 = k_{21}x_1 + k_{22}x_2 + \ldots + k_{2p}x_p \\ \quad \ldots \\ Z_m = k_{m1}x_1 + k_{m2}x_2 + \ldots + k_{mp}x_p \end{cases} \tag{9}$$

where $x_1, x_2, \ldots, x_p$ are the original variants, and the subscript p is the number of variants. $Z_1, Z_2, \ldots, Z_m$ are the new variants, i.e., the principal components, and the subscript m is the number of new variants. k_{mp} is the load coefficients. For the m and p, their relationship is $m \leq p$.

In this work, the cumulative contribution rates of different principal components were computed, which are shown in Fig. 13.

In Fig. 13, the cumulative contribution rates of all principal components are larger than 80 %. With the increase in the principal components, the cumulative contribution rates also increase. In this work, to retain the original characteristic information of photoacoustic peak-to-peak spectra of real and fake blood as long as possible, a cumulative contribution rate of 95 % was used to choose the principal components. Under four kinds of different principal components, the effects of the neuron number in the hidden layer and two learning rate factors on the correct rates of classification and discrimination for real and fake blood based on the PCA-WNN-PSO algorithm were studied, which are shown in Fig. 13(a)–(c), respectively.

In Fig. 14(a), with the increase in principal components from 6 to 10, the correct rates increase under different numbers of neurons in the hidden layer. For the principal components of 10, the best correct rate reaches 100 % under 10 neurons of the hidden layer. However, when the principal components increase to 12, the best correct rates corresponding to 11 and 13 neurons numbers of hidden layer are 93.3 %. For the learning rate factor η, in Fig. 14(b), the correct rates corresponding to the principal components of 10 are superior to those of three others, especially for the learning rate factor η =0.001, where the correct rate of 10 principal components reaches 100 %. For another learning rate factor λ, in Fig. 14(c), the correct rates of the 10 principal components are higher than those of the three others when the learning rate factor λ is 0.04, and the correct rate of the PCA-WNN-PSO algorithm reaches 100 %.

The effects of iteration times on the correct rate under different principal components based on the PCA-WNN-PSO algorithm were obtained, which are shown in Fig. 15(a). In Fig. 15(a), with the increase in iteration times from 6 to 10, the correct rates increase for all principal components. For the principal components of 10, when the number of iterations is 108, the correct rate reaches 100 %. However, when the number of principal components increases to 12, the correct rate decreases to 93.3 % at 121 iterations. Therefore, the correct rate and number of iterations of the 10 principal components are satisfactory. Fig. 15(b) gives the mean square error curves of four kinds of different principal components in the training process of the PCA-WNN-PSO algorithm. From Fig. 15(b), it can be seen that for all principal components, the mean square errors all decrease with increasing training times. Moreover, the mean square errors decrease with the increase in principal components. To better compare the performances of different principal components, the prediction results of 30 test blood samples under four kinds of different principal components based on the PCA-WNN-PSO algorithm were obtained, which are shown in Fig. 15(c). In Fig. 15(c), the correct rate of the 6 principal components is not satisfactory (i.e., 83.3 %), and four classification errors occur in three kinds of real blood, i.e., cow blood, rabbit blood, and sheep blood. For 8 principal components, there was one fake blood, i.e., props blood, that was misjudged to be red ink. The correct rate of the 8 principal components is 96.7 %. For the 12 principal components, there was one fake blood of red ink misjudged to be prop blood, and its correct rate was also 96.7 %. However, for 10 principal components, the classification and discrimination of all real and fake blood samples are correct, i.e., the correct rate reaches 100 %. Therefore, the performance of principal component number 10 based on the PCA-WNN-PSO algorithm is the best.

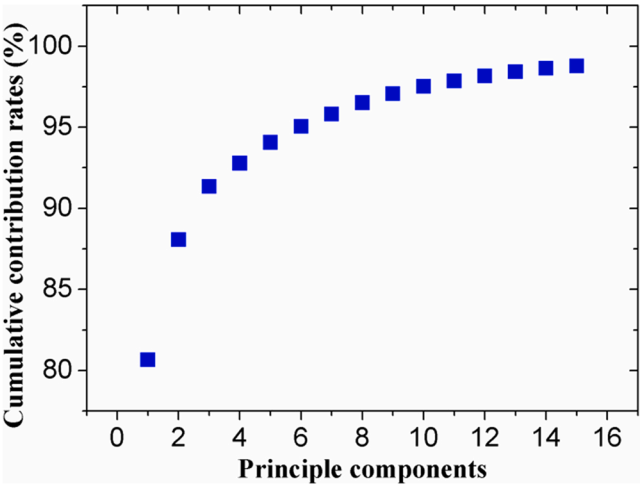

Fig. 13. Cumulative contribution rates of different principal components.

4.3. Comparison results of different algorithms

Finally, the classification and discrimination performances for real and fake blood were compared by using seven different algorithms. Five kinds of algorithms are supervised classification and recognition algorithms, i.e., extreme learning machine (ELM) [34], SVM [35], WNN, WNN-PSO, and PCA-WNN-PSO with 10 principal components. In addition, two kinds of unsupervised classification and recognition algorithms were used, i.e., competitive neural network (CNN) [36] and self-organizing map neural network (SOMNN) [37]. The correct rates based on these seven kinds of algorithms are shown in Fig. 16.

In Fig. 16, for two kinds of unsupervised algorithms (i.e., CNN and SOMNN), their correct rates are less than those of the supervised algorithms. However, for the simple WNN algorithm, its correct rate is not satisfied, which is less than those of other algorithms. However, for the WNN optimized by the PSO algorithm, i.e., the WNN-PSO algorithm, its correct rate is greatly improved, which is 96.7 % and larger than those of the ELM algorithm and SVM algorithm. For the PCA-WNN-PSO algorithm, the correct rate is further improved to 100 % when the principal components are 10.

5. Conclusion

The rapid and accurate identification of real and fake blood is very important in such fields as biomedicine, food safety, and criminal investigation. To achieve this goal, photoacoustic spectroscopy was used to establish a blood detection system. The time-resolved photoacoustic signals of six different kinds of real and fake blood with 150 groups in total were captured at 700−1064 nm with 5 nm intervals, as well as the PPVs. To achieve a high classification and discrimination rate, the WNN algorithm was used. At the same time, the PSO algorithm was used to optimize the weights, thresholds, translation factor and scale factor of the wavelet basis function of the WNN. For the WNN and WNN-PSO algorithms, the effects of the parameters of both algorithms on the correct rate were investigated. Meanwhile, the LDIW strategy was used to modify the inertia weight of the PSO algorithm. Then, the PCA algorithm was combined into the WNN-PSO algorithm to further improve the correct rate. The effect of different principal components on the correct rate based on the PCA-WNN-PSO algorithm was studied. Finally,

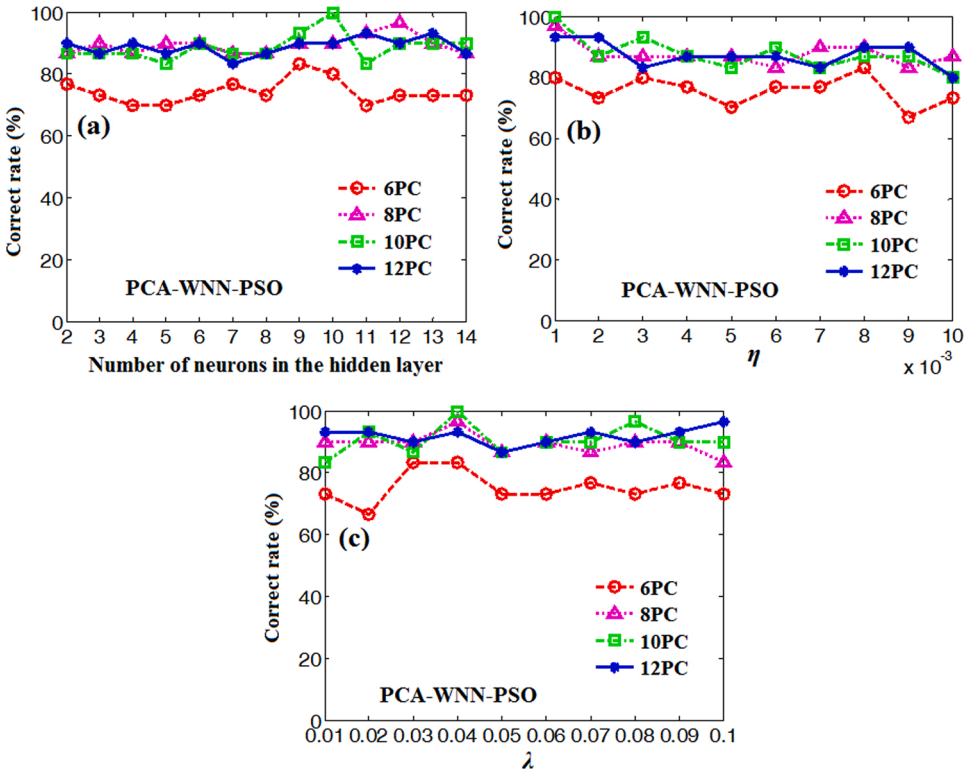

Fig. 14. The effects of four different principal components on the correct rate of classification and discrimination for real and fake blood based on PCA-WNN-PSO algorithm. (a) the number of neurons in the hidden layer; (b) the learning factor η; (c) the learning factor.

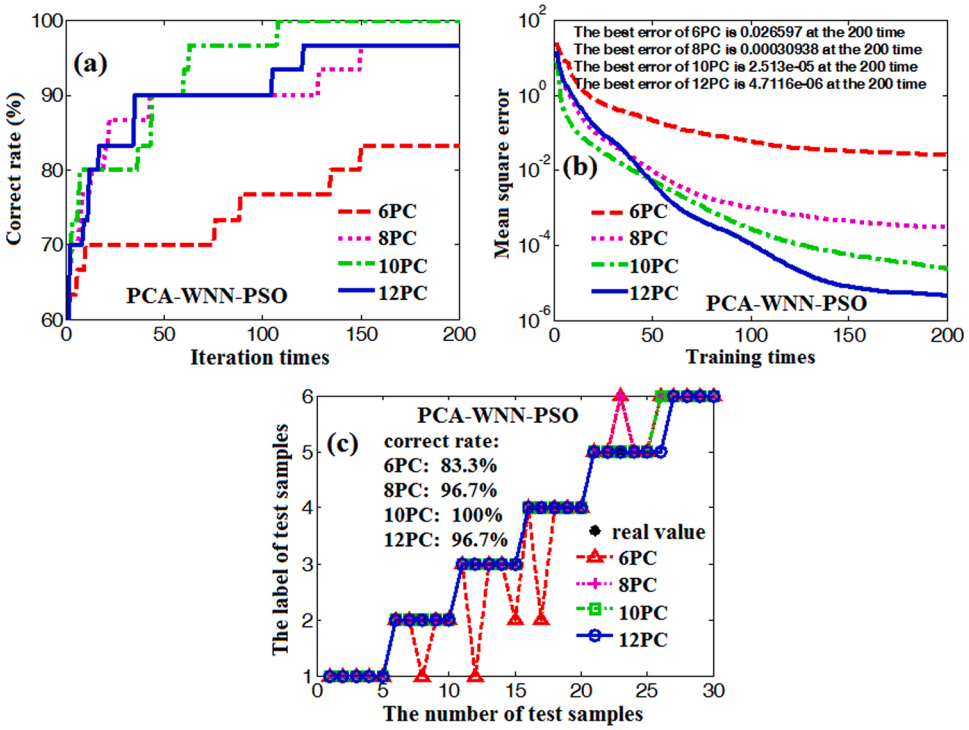

Fig. 15. (a) Comparison results of different principal components for the iteration times, (b) training times, and (c) predicted results of test samples.

the performances of seven different algorithms were compared. The results show that (1) the amplitudes, profiles, peak-point time, and PPVs between real and fake blood are different at some wavelengths, but the spectral overlaps of PPVs impact the accurate classification and discrimination of real and fake blood, which is the purpose of using WNN algorithms to improve the correct rate. (2) Compared with the WNN algorithm, under the optimal parameters, the correct rate was improved by 33.4 % via the WNN-PSO algorithm. At the same time, the correct rate of the WNN-PSO algorithm with the LDIW strategy is superior to that of the fixed inertia weight. (3) The correct rate of the PCA-

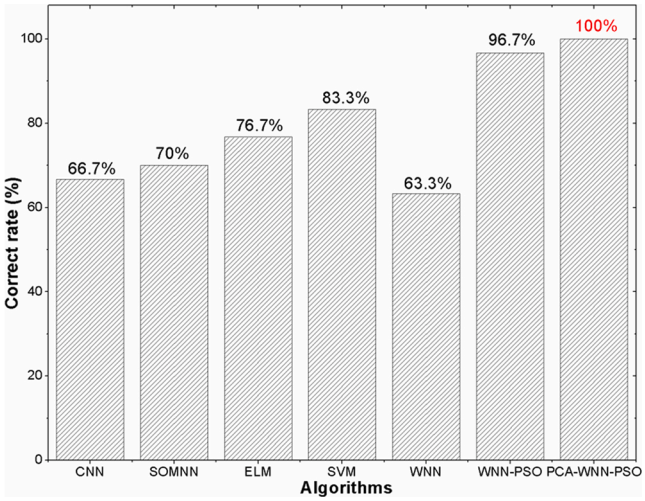

Fig. 16. Correct rates of classification and discrimination for real and fake blood based on different algorithms.

WNN-PSO algorithm with 10 principal components reached 100 %, and the mean square error at 200 training iterations was improved by approximately 99.8 %. Moreover, the number of iterations corresponding to the largest correct rate also decreased from 126 to 108. (4) The comparison results of seven different algorithms show that the highly accurate classification and discrimination of real and fake blood can be significantly achieved by using photoacoustic spectroscopy combined with the PCA-WNN-PSO algorithm.

Funding information

This work was supported by the Chinese National Natural Science Fund Project (No. 61650402, No. 51763011), Innovation of Outstanding Young Personnel Training Program of Jiangxi Province (No. 20192BCBL23015), Young top-notch personnel fund project of JXSTNU (No. 2014QNBJRC004), and the project of Key Laboratory of Optic-electronic Detection and Information Processing of Nanchang City (No. 2019-NCZDSY-008).

Declaration of Competing Interest

The authors declare that there are no conflicts of interest.

References

[1] R.H. Bremmer, G. Edelman, T.D. Vegter, T. Bijvoets, M.C.G. Aalders, Remote spectroscopic identification of blood stains, J. Forensic Sci. 56 (2011) 1471–1475.
[2] G.J. Edelman, Spectral Analysis of Blood Stains at the Crime Scene, PhD thesis, University of Amsterdam, The Netherlands, 2014.
[3] N. Archana, C. Rita, N. Manjunath, B. Maya, R.C. Sadanandavalli, Liquid chromatography-tandem mass spectrometry method for estimation of a panel of lysophosphatidylcholines in dried blood spots for screening of X-linked adrenoleukodystrophy, Clin. Chim. Acta 485 (2018) 305–310.
[4] M. Prata, A. Ribeiro, D. Figueirinha, R. Tiago, O. David, R. José, R.T.S.A. André, C. Suzel, B. Mário, G. Eugenia, Determination of opiates in whole blood using microextraction by packed sorbent and gas chromatography-tandem mass spectrometry, J. Chromatogr. A 1602 (2019) 1–10.
[5] A. Gloria, M.C. Veronesi, R. Carluccio, P. Salvatore, D.A. Ippolito, C. Alberto, Biochemical blood analysis along pregnancy in Martina Franca jennies, Theriogenology 115 (2018) 84–89.
[6] X. Wan, J. Wang, P.X. Liu, T.T. Zhang, Identification of animal whole blood based on near infrared transmission spectroscopy, Spectrosc. Spect. Anal. 36 (2016) 80–83.
[7] P.L. Bai, J. Wang, H.C. Yin, Y.B. Tian, W.M. Yao, J. Gao, Rapid qualitative identification method of species of blood based on PCA with Raman spectroscopy, J. Light Scat. 28 (2016) 163–167.
[8] G. Mclaughlin, K.C. Doty, I.K. Lednev, Discrimination of human and animal blood traces via Raman spectroscopy, Forensic Sci. Int. 238 (2014) 91–95.
[9] N. Wang, C. Wang, H.Y. Bian, J. Wang, P. Wang, P.L. Bai, H.C. Yin, Y.B. Tian, J. Gao, The identification method of blood by applying Hilbert transform to extract phase information of Raman spectra, Spectrosc. Spect. Anal. 38 (2018) 2412–2418.
[10] B. Gao, P.F. Zhao, Y.X. Lu, Y. Fan, L.H. Zhou, J. Qian, L.N. Liu, S.Y. Zhao, Z. F. Kong, Study on recognition and classification of blood fluorescence spectrum with BP neural network, Spectrosc. Spect. Anal. 38 (2018) 3136–3143.
[11] P.F. Lu, Y. Fan, L.H. Zhou, J. Qian, L.N. Liu, S.Y. Zhao, Z.F. Kong, B. Gao, Feature extraction and classification of animal blood spectra with support vector machine, Spectrosc. Spect. Anal. 37 (2017) 3828–3832.
[12] Z. Ren, G.D. Liu, Z. Huang, D.J. Zhao, Z.H. Xiong, Exploration and practice in photoacoustic measurement for glucose concentration based on tunable pulsed laser induced ultrasound, Int. J. Optomechatroni. 9 (2015) 221–237.
[13] Z. Ren, G.D. Liu, Z. Huang, Z.H. Xiong, Non-invasive detection of blood glucose concentration based on photoacoustic spectroscopy combined with principle component regression method, Spectrosc. Spect. Anal. 36 (2016) 1674–1679.
[14] T. Yujiro, T. Takuro, S. Michiko, W. Kayo, Differential continuous wave photoacoustic spectroscopy for non-invasive glucose monitoring, IEEE Sens. J. 20 (2019) 4453–4458.
[15] R. Hochuli, L. An, P.C. Beard, B.T. Cox, Estimating blood oxygenation from photoacoustic images: can a simple linear spectroscopic inversion ever work? J. Biomed. Opt. 24 (2019) 1–13.
[16] J. Chen, Y. Zhang, L. He, Y.Z. Liang, L.D. Wang, Wide-field polygon-scanning photoacoustic microscopy of oxygen saturation at 1-MHz A-line rate, Photoacoustics 20 (2020), 100195.
[17] C. Liu, Y. Liang, L. Wang, Single-shot photoacoustic microscopy of hemoglobin concentration, oxygen saturation, and blood flow in sub-microseconds, Photoacoustics 17 (2020), 100156.
[18] M. Yang, L.Y. Zhao, F. Yang, M. Wang, N. Su, C.Y. Zhao, Y. Gui, Y. Wei, R. Zhang, J. C. Li, T. Han, X.J. He, L. Zhu, H.W. Wu, C.H. Li, Y.X. Jiang, Quantitative analysis of breast tumours aided by three-dimensional photoacoustic/ultrasound functional imaging, Sci. Rep. 10 (2020) 8047.
[19] T. Han, M. Yang, F. Yang, L.Y. Zhao, Y.X. Jiang, C.H. Li, A three-dimensional modeling method for quantitative photoacoustic breast imaging with handheld probe, Photoacoustics 21 (2021), 100222.
[20] C.K.N. Patel, A.C. Tam, Pulsed optoacoustic spectroscopy of condensed matter, Rev. Mod. Phys. 53 (1981) 517–550.
[21] J. Xie, W. Chen, H. Dai, Distributed cooperative learning algorithms using wavelet neural network, Neural Comput. Appl. 31 (2019) 1007–1021.
[22] Z.Y. Cao, N. Guo, M.H. Li, K.L. Yu, K.Q. Gao, Back propagation neutral network based signal acquisition for brillouin distributed optical fiber sensors, Opt. Express 27 (2019) 4549–4561.
[23] R.J.E. Merry, Wavelet Theory and Applications: a Literature Study, Technische Universiteit Eindhoven, Eindhoven, 2005, pp. 1–41.
[24] Y. Shi, R. Eberhart, Parameter selection in particle swarm optimization, in: Evolutionary Programming VII: Proc. EP 98, New York: Springer Verlag, 1998, pp. 591–600.
[25] A.A. Martins, O.A. Aderemi, On the performance of linear decreasing inertia weight particle swarm optimization for global optimization, Sci. World J. 2013 (2013) 1–12.
[26] Z.W. Cheng, H.G. Ma, Z.Y. Wang, S.H. Yang, In vivo volumetric monitoring of revascularization of traumatized skin using extended depth-of-field photoacoustic microscopy, Front. Optoelectron. 13 (2020) 307–317.
[27] K.S. Ratan, R. Madhusudan, K. Subhajit, H. Eno, C.K. Michael, Validity of a theoretical model to examine blood oxygenation dependent optoacoustics, J. Biomed. Opt. 17 (2012), 055002.
[28] X. Geng, S. Lu, M. Jiang, Q. Sui, S. Lv, H. Xiao, Y. Jia, L. Jia, Research on FBG-based CFRP structural damage identification using BP neural network, Photonic Sens. 8 (2018) 168–175.
[29] C. Ren, N. An, J. Wang, L. Li, B. Hu, D. Shang, Optimal parameters selection for BP neural network based on particle swarm optimization: a case study of wind speed forecasting, Knowl. Based Syst. 56 (2014) 226–239.
[30] Z.Y. Li, L. Ma, H.Z. Zhang, Quantum bat algorithm for function optimization, J. Syst. Manag. 21 (2014) 717–722.
[31] A. Carlisle, G. Dozier, An off-the-shelf PSO, in: Proceedings of the Workshop on Particle Swarm Optimization 2001, Indianapolis, 2001.
[32] X.T. Yu, W.X. Lu, F.L. Chu, Rotating machinery fault diagnosis based on fuzzy proximal support vector machine optimized by particle swarm optimization, J. Vibrat. Shock 28 (2009), 183-133.
[33] N. Kambhatla, T.K. Leen, Dimension reduction by local principal component analysis, Neural Comput. 9 (1997) 1493–1516.
[34] G.B. Huang, Q.Y. Zhu, C.K. Siew, Extreme learning machine: theory and applications, Neurocomputing 70 (2006) 489–501.
[35] X. Tan, F. Yu, X. Zhao, Support vector machine algorithm for artificial intelligence optimization, Cluster Comput. 22 (2019) 15015–15021.
[36] E. Lotfi, A.A. Rezaee, A competitive functional link artificial neural network as a universal approximator, Soft Comput. 22 (2018) 4613–4625.
[37] R. Zhu, J. Wang, T. Qiu, S. Sui, Y.J. Han, Y.X. Jia, Y.F. Li, M.B. Yan, Y.Q. Pang, Z. Xu, S.B. Qu, Overcome chromatism of metasurface via greedy algorithm empowered by self-organizing map neural network, Opt. Express 28 (2020) 35724.

Zhong Ren received his Doctor degree in June 2017 from Nanchang University. He is currently a professor in Key Laboratory of Optic-electronics and Communication, Jiangxi Science and Technology Normal University. He focuses on the researches of the non-invasive detection of photoacoustic spectroscopy and its application in biomedical fields.

Tao Liu received his Bachelor degree in June 2019 from Jiangxi Science and Technology Normal University. He is currently a master student in Key Laboratory of Optic-electronics and Communication, Jiangxi Science and Technology Normal University. He focuses on the researches of the non-invasive detection of photoacoustic spectroscopy.

Guodong Liu received his Doctor degree in June 2004 from Tsinghua University. He is currently a professor in Key Laboratory of Optic-electronics and Communication, Jiangxi Science and Technology Normal University. His research interest includes the optical engineering, photoacoustic spectroscopy, photoacoustic imaging and its application in biomedical fields.